

**NASA TECHNICAL
REPORT**

NASA TR R-192



NASA TR R-192

C.1

LOAN COPY: F
AFWL (W
KIRTLAND AF

0068073



TECH LIBRARY KAFB, NM

**THERMAL AND THERMIONIC
CHARACTERISTICS OF A LARGE-SCALE
EXPERIMENTAL THERMIONIC CONVERTER**

by A. Vary

Lewis Research Center

Cleveland, Ohio



**THERMAL AND THERMIONIC CHARACTERISTICS OF A
LARGE-SCALE EXPERIMENTAL
THERMIONIC CONVERTER**

By A. Vary

**Lewis Research Center
Cleveland, Ohio**

NATIONAL AERONAUTICS AND SPACE ADMINISTRATION

**For sale by the Office of Technical Services, Department of Commerce,
Washington, D.C. 20230 -- Price \$1.00**

THERMAL AND THERMIONIC CHARACTERISTICS OF A
LARGE-SCALE EXPERIMENTAL
THERMIONIC CONVERTER

by A. Vary

Lewis Research Center

SUMMARY

A thermionic energy converter based on a coaxial diode configuration was used to obtain information relative to problems associated with instrumenting and heating a large-scale converter and to determine certain thermal and thermionic characteristics. The cylindrical tungsten cathode, having an emitting area of 73.7 square centimeters, was operated at temperatures in the range 1200° to 2000° K. Diode thermal characteristics such as temperature gradients, temperature ratios, heat-flow distributions, and thermal emissivities were studied. Thermionic characteristics were determined in both a vacuum and a cesium vapor atmosphere. The investigation defined problems associated with thermal gradients on emitting areas, interelectrode resistive leakage caused by vapor deposition, determination of heat-transfer properties, and measurement of cathode emission properties.

INTRODUCTION

There is a need for reliable, lightweight, long-life space power systems for auxiliary and propulsion power. Systems based on thermionic energy conversion have attracted much attention as a means of satisfying space power requirements (refs. 1 and 2); parametric studies have shown them to be potentially competitive with other more fully developed schemes such as the turboelectric-generator power system (ref. 3).

Thermionic methods of energy conversion have been studied extensively (refs. 4 to 15). In general, these studies have involved planar and coaxial cylindrical configurations with interelectrode spacings of 0.01 to 3.00 millimeters and emitting areas approaching 25 square centimeters. Thermionic outputs have ranged up to 30 watts per square centimeter for cathode operating temperatures up to 2500° K. Electrically energized cathode heaters using resistance or electron bombardment have been widely employed, although radioisotope and fission heat sources have been used in many studies to simulate feasible energy sources for space applications.

This report describes an experimental thermionic converter which was used to obtain information relative to problems associated with the heating and instrumentation of a large-scale diode converter. The sizes of the converter and its component parts were chosen to facilitate instrumentation and the measurement of pertinent thermal and electronic characteristics. (This investigation was not concerned with the improvement of the conversion efficiency, which was actually quite low because of the operating conditions used.)

The converter used in this experiment was based on a coaxial cylindrical diode configuration in which a pure tungsten cylinder was used as the cathode. The cathode emitting area was 73.7 square centimeters, and the interelectrode radial spacing between the cathode and the surrounding anode was 2.8 millimeters.

The cathode was heated by radiant heat transfer from an enclosed coaxial refractory metal heater, which was operated at power inputs up to 3 kilowatts. Because of the large size of the diode, the heater was not isolated from the cathode as is usual in experimental thermionic devices. Hence, the heater might have contributed electrons to the interelectrode space and thus affected the output efficiency. Inasmuch as the main purpose of this investigation was not the determination of efficiency, however, and because of design difficulties, it was deemed unnecessary to isolate the heater.

Pyrometric measurements were made to determine electrode temperature at various heater power inputs and to determine temperature profiles and gradients along electrodes and other components. Calorimetric measurements were made to determine heat-flow distribution along various radiative and conductive channels and to gauge the thermal emissivities of the electrodes.

Thermionic properties such as work function and emission constant were determined along with thermionic output characteristics for vacuum and a cesium-vapor atmosphere.

DESCRIPTION OF APPARATUS

Structure of Converter

The converter consisted of two coaxial cylindrical electrodes, as illustrated in figure 1. The cathode (fig. 2) was formed from unalloyed, high-purity sintered tungsten plate and the anode (fig. 3) from annealed, high-purity tantalum plate. The radial spacing between the cathode and the anode was 2.8 millimeters, and the emitting area of the cathode was 73.7 square centimeters.

As shown in figure 4, support structures positioning and constraining the electrodes also provided electrical paths leading to external circuitry. Supports immediately adjacent to the electrodes consisted of radial members about 3 centimeters in length and 1 square centimeter in cross-sectional area. Tantalum was used for the supports; the contact resistance with the electrodes measured less than 0.01 ohm. Radiation shields consisting of 0.01-inch-wall

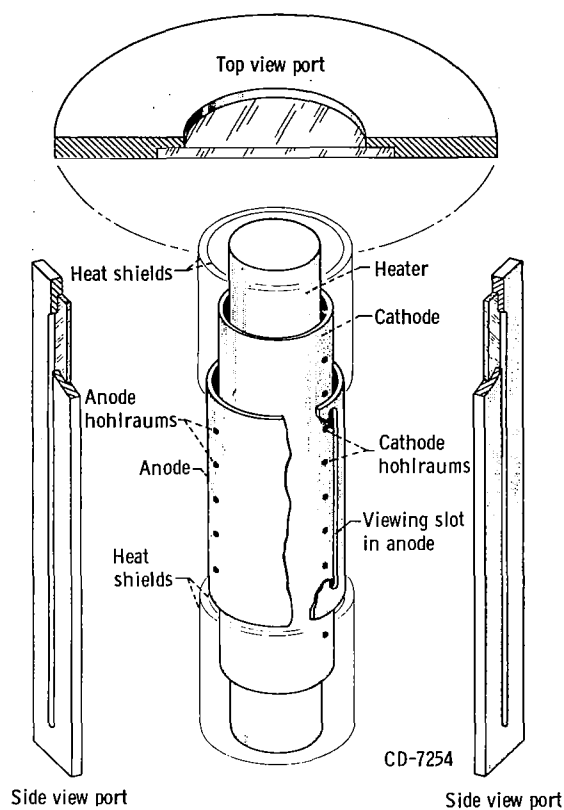


Figure 1. - Electrode configuration.

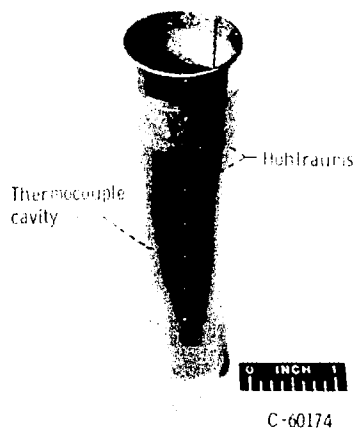


Figure 2. - Pure-sintered-tungsten cathode. Outside diameter, 3.08 centimeters; wall thickness, 1.5 millimeters; overall length, 12.9 centimeters; emitting area, 73.7 square centimeters.

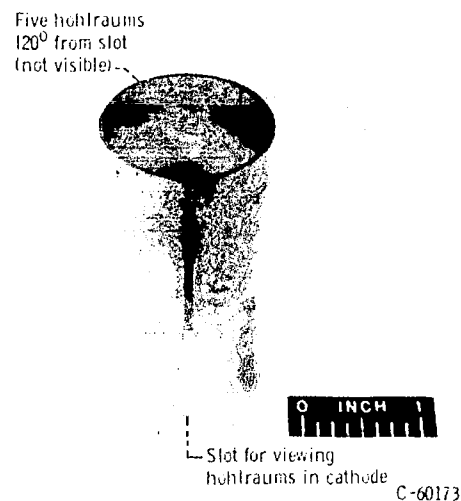


Figure 3. - High-purity-tantalum anode. Outside diameter, 3.90 centimeters; wall thickness, 1.3 millimeters; overall length, 7.6 centimeters.

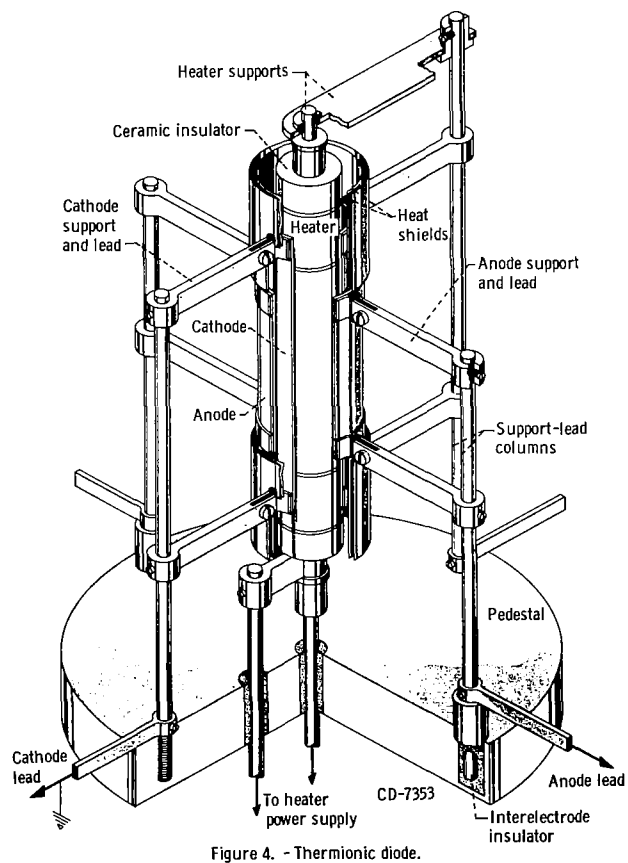


Figure 4. - Thermionic diode.

tantalum cylinders, which were essentially continuations of the anode cylinder, were provided to reduce end heat losses.

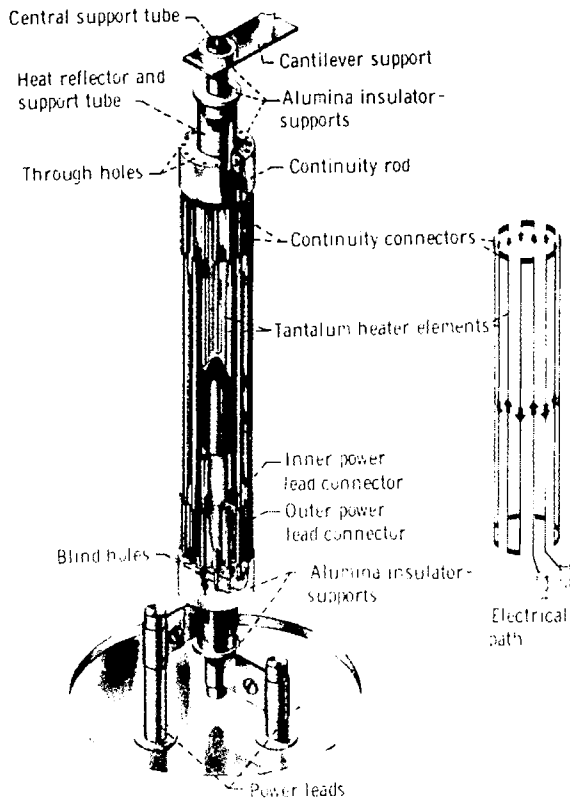


Figure 5. - Cathode heater.

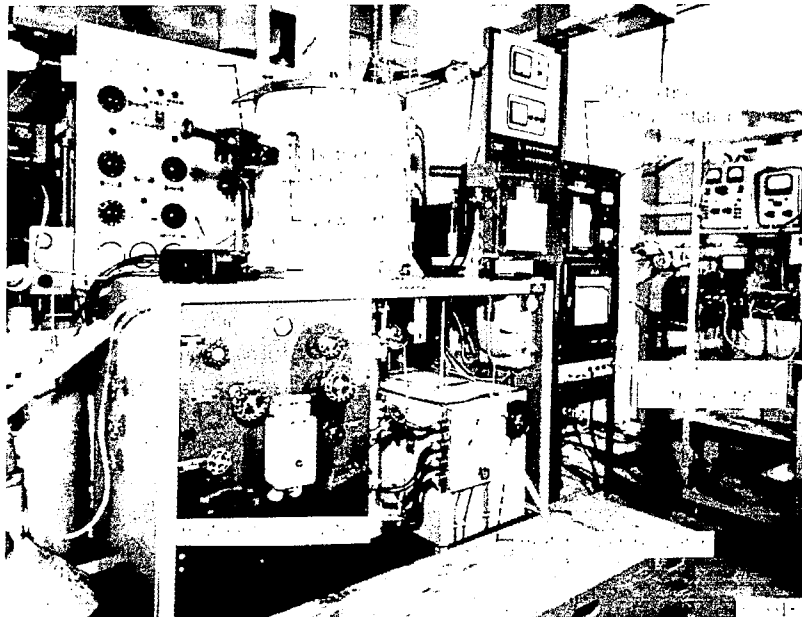
CD-7272

The cathode heater, which consisted of tantalum and ceramic components, is illustrated in figure 5; details of heater construction and operating characteristics are presented in appendix B.

Associated Equipment

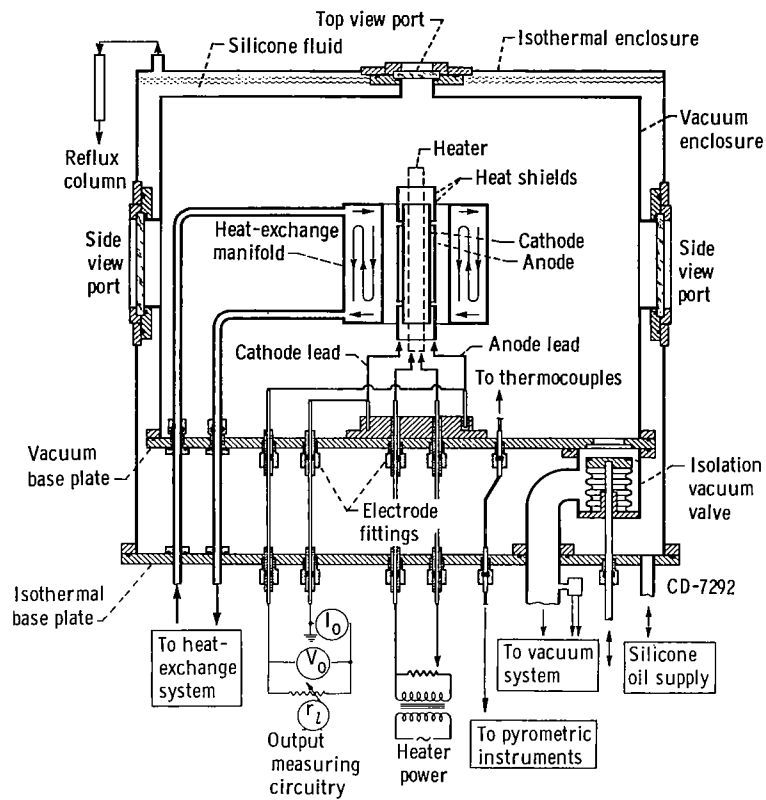
Vacuum enclosure. - The vacuum enclosure consisted of a stainless-steel cylindrical chamber 15 inches high and 15 inches in diameter mounted on a circular base plate. (A photograph of the experimental setup appears in figure 6(a).) The salient features of the vacuum enclosure and associated parts are illustrated diagrammatically in figure 6(b).

The vacuum chamber contained three ports for viewing the converter assembly; two were located on the sides of the chamber for radial viewing, and one was located at the top of the chamber for axial viewing.



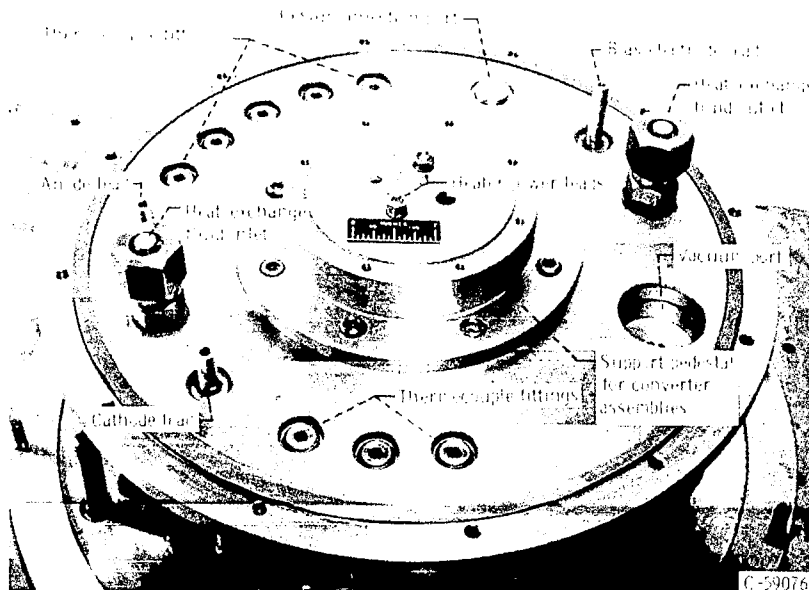
(a) Overall view.

Figure 6. - Thermionic converter experimental setup.



(b) Vacuum chamber.

Figure 6. - Continued. Thermionic converter experimental setup.



(c) Vacuum base plate.

Figure 6. - Concluded. Thermionic converter experimental setup.

The vacuum base plate, figure 6(c), contained the vacuum port; a number of penetrations for electrical leads, thermocouples, and hydraulic lines; and the cesium injection port.

A second larger chamber, designated as the isothermal enclosure, was provided to contain the vacuum enclosure, as indicated diagrammatically in figure 6(b). The space between the vacuum and isothermal enclosures was filled with silicone fluid, which was heated during the cesium-vapor operations to control the vapor pressure. Because uniformity of temperature at all points of the vacuum enclosure could not be ensured, certain regions such as the view ports were maintained at slightly elevated temperatures. With this precaution, the temperature of the coldest region was essentially the same as that of the isothermal silicone fluid.

Heat-exchange system. - A heat-exchange system (fig. 6(b)) was used to determine the heat-flow distribution. A heat-exchange manifold, installed only during the heat-balance experiments, absorbed heat radiated by a mock converter. The mock converter was so constructed that heat dissipated along various heat-flow paths could be gaged by calculating the quantity of radiant heat absorbed by the manifold and the quantities of heat conducted away through the electrode and the heater leads and supports. The heat-exchange system is described in detail in appendix C.

RESULTS

Thermal Characteristics

Temperature characteristics. - Relations between electrode and heater temperatures and heater input power are shown in figure 7, in which T_c , T_a , and

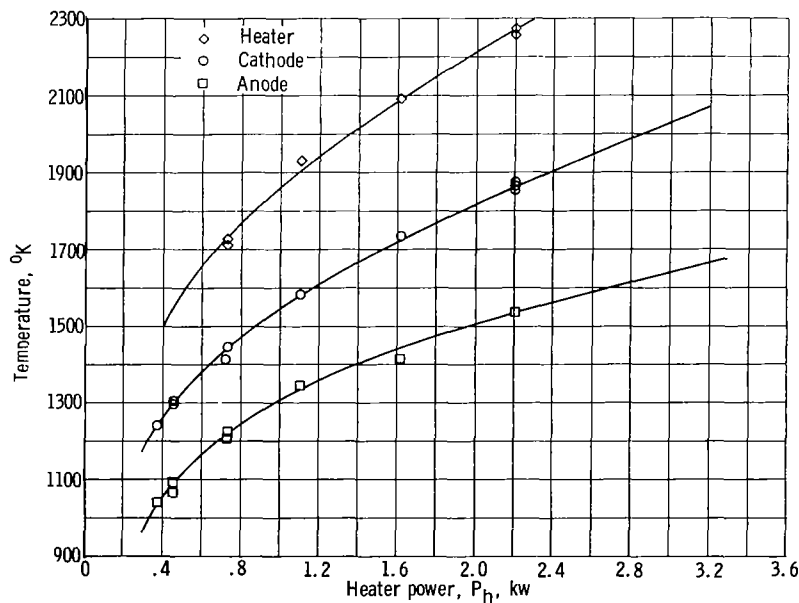


Figure 7. - Temperature-power characteristics.

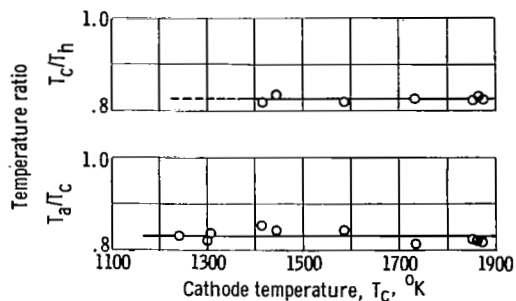


Figure 8. - Temperature ratios.

T_h are plotted against heater input power P_h . (Symbols are defined in appendix A.) Appendix D describes the methods used to determine electrode and heater temperatures. Figure 8 shows temperature ratios T_a/T_c and T_c/T_h for a series of cathode temperatures T_c ranging from 1200° to 2000° K. Temperature gradients measured axially along the electrode cylinders at various levels of heater power are shown in figure 9.

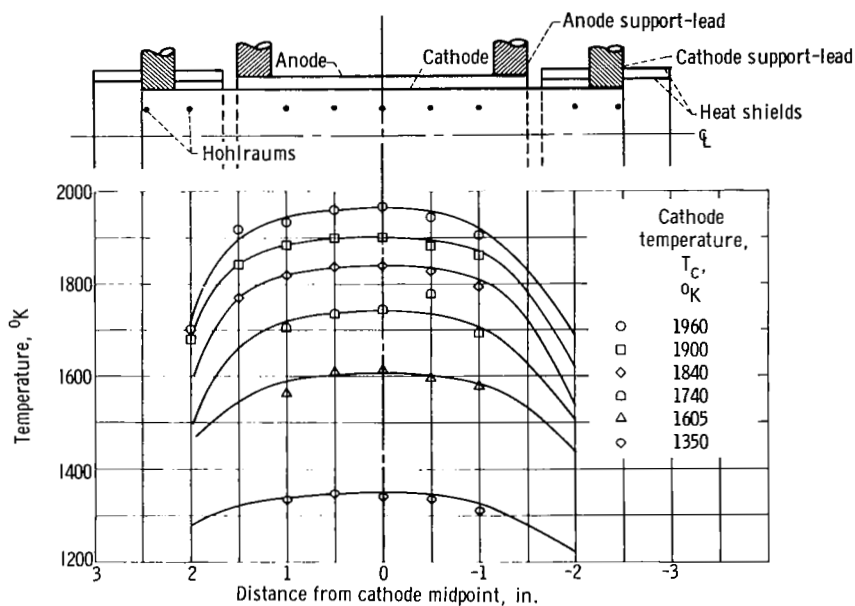


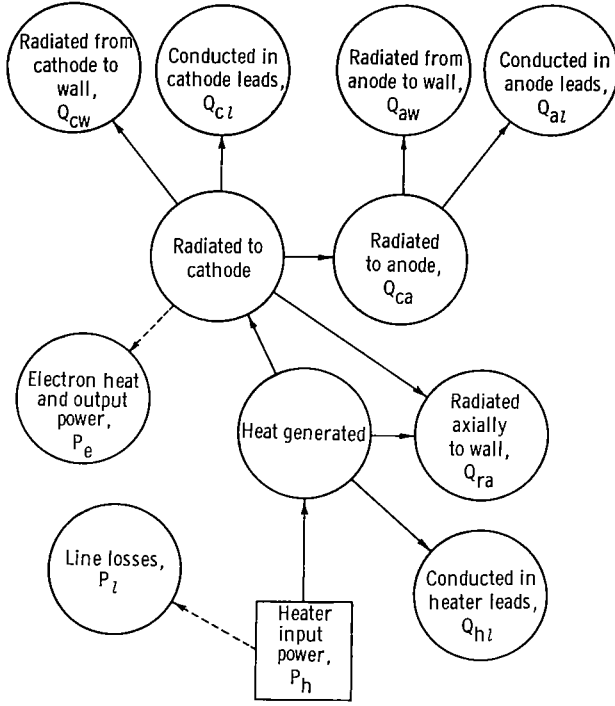
Figure 9. - Cathode temperature profile.

Heat-flow distribution. - The heat-flow distribution is illustrated schematically in figure 10. The relation between heater input power and heat flows along various paths may be expressed as

$$P_h = Q_{hl} + Q_{ra} + Q_{cl} + Q_{cw} + Q_{al} + Q_{aw} + P_e + P_l \quad (1)$$

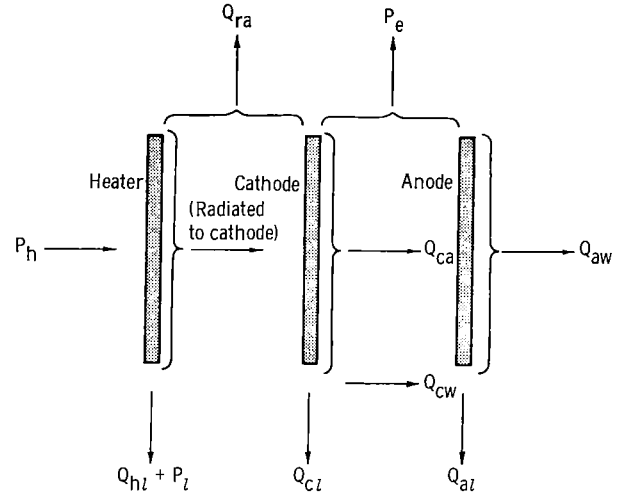
If the heat flow in the leads and the heat radiated radially are combined and if it is noted that for the operating conditions used in this experiment both P_e and P_l are negligible compared with the other quantities, equation (1) may be rewritten as

$$P_h = Q_l + Q_m + Q_{ra} \quad (2)$$



(a) Diagram of distribution.

Figure 10. - Heat-flow distribution.



(b) Schematic of heat flow.

Figure 10. - Concluded. Heat-flow distribution.

where

$$Q_l = Q_{hl} + Q_{cl} + Q_{al} \quad (3)$$

and

$$\left. \begin{aligned} Q_m &= Q_{cw} + Q_{aw}, & Q_{cw} &= \alpha Q_m, \\ Q_{aw} &= \beta Q_m, & \alpha + \beta &= 1 \end{aligned} \right\} \quad (4)$$

The heat conducted away through leads and supports Q_l was calculated from measured temperature differences, physical dimensions such as lengths and cross sections, and thermal conductivities. The heat radiated radially from the converter Q_m was calculated from measurements made by means of the heat-exchange manifold described in appendix C. The heat radiated axially from the converter assembly Q_{ra} was calculated as the difference between P_h and $Q_m + Q_l$. The constants α and β were determined from converter geometry and temperature profiles to express the fractions of Q_m , which appeared as Q_{cw} and Q_{aw} . Heat flows determined from these measurements and calculations are given in table I.

TABLE I. - DISTRIBUTION OF HEAT FLOW

Heater power, P_h , kw	Cathode temperature, T_c , °K	Mode of heat flow							
		Conduction through leads, Q_l		Axial radiation, Q_{ra} (a)		Radial radiation, Q_m (b)			
						Cathode to wall, Q_{cw}		Anode to wall, Q_{aw}	
		Per-cent	kw	Per-cent	kw	Per-cent	kw	Per-cent	kw
0.5	1350	28	0.13	21	0.10	21	0.11	30	0.15
1.0	1570	17	.17	13	.15	29	.29	41	.41
1.5	1730	13	.20	10	.16	32	.45	45	.65
2.0	1860	12	.23	8.8	.17	32	.66	47	.94
2.5	1970	11	.24	7.1	.18	33	.90	48	1.2
3.0	2090	11	.26	6.2	.18	34	1.0	49	1.5

^aIncludes axial radiation from both heater and cathode.

^bEssentially radial radiation (measured with heat-exchange manifold, calculated by means of eq. (C1), appendix C).

Thermionic Characteristics

Cathode emission properties. - In order to determine cathode work function and emission constant, positive voltages V_p were applied to the anode to draw plate current from the cathode. Figure 11 shows plate current drawn by the anode I_p against V_p for a series of cathode temperatures. Saturation current density J_s plotted against T_c for the tungsten cathode is shown in figure 12. The Richardson-Dushman plot of $\ln(J_s/T_c^2)$ against $1/T_c$ shown in figure 13 was used to obtain the work function ϕ_c and the variation of ϕ_c with T_c in figure 14.

Output characteristics. - Output currents were determined for cathode temperatures between 1500° and 2000° K. The load r_l consisted of a series of calibrated resistors variable from 1 ohm to 1 megohm in increments following a logarithmic sequence. Output currents I_o were calculated by means of output voltages V_o measured across r_l with an electrometer.

For convenience in presenting the mathematical analysis in the DISCUSSION OF RESULTS, the convention that output (or anode) voltages be considered positive was adopted in plotting the output characteristics. (In a converter, under output conditions, the anode polarity is actually negative.)

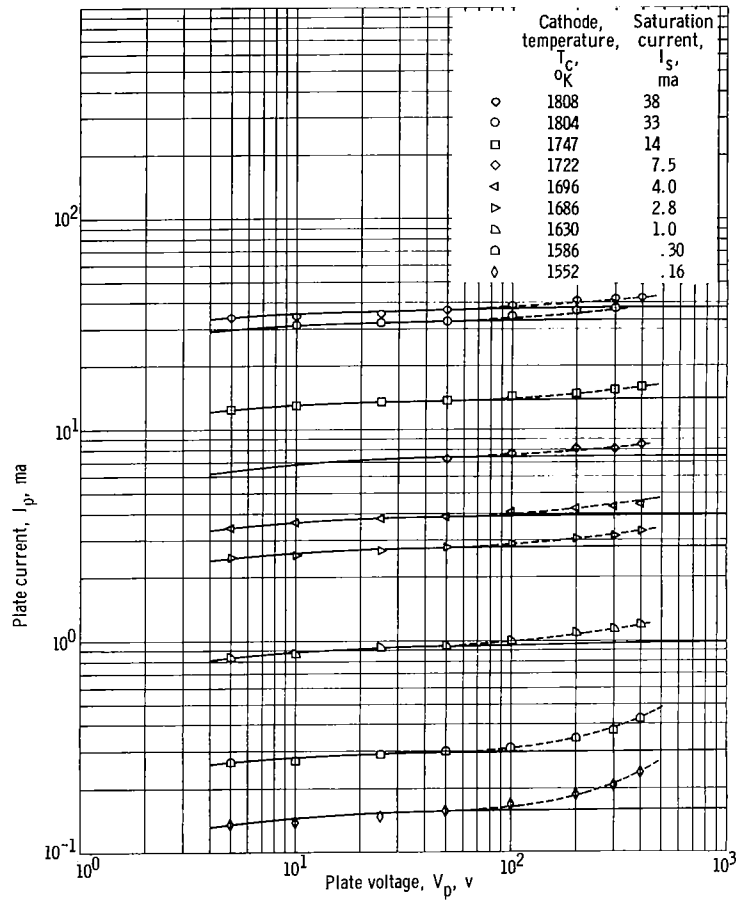


Figure 11. - Voltage saturation curves.

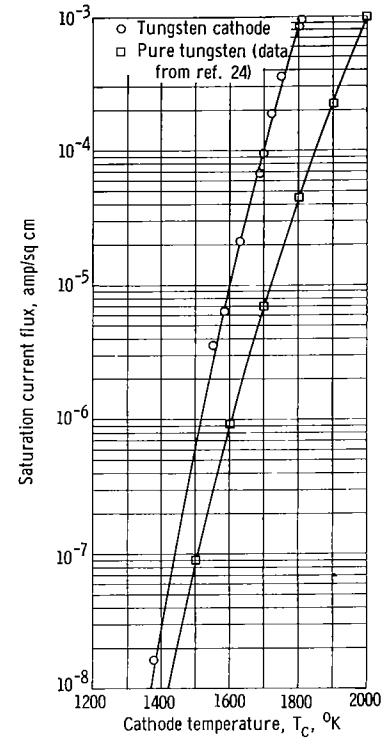


Figure 12. - Saturated emission current density for tungsten cathode.

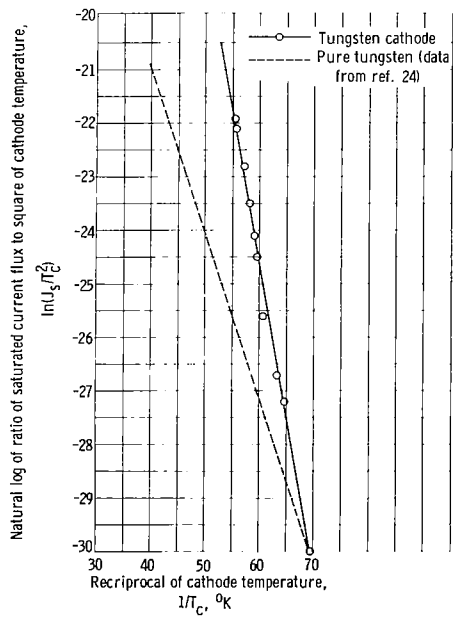


Figure 13. - Richardson-Dushman plot for tungsten cathode.

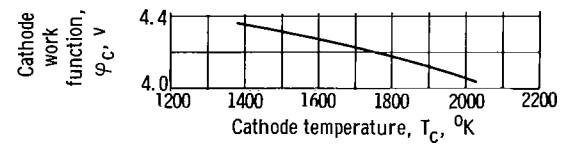
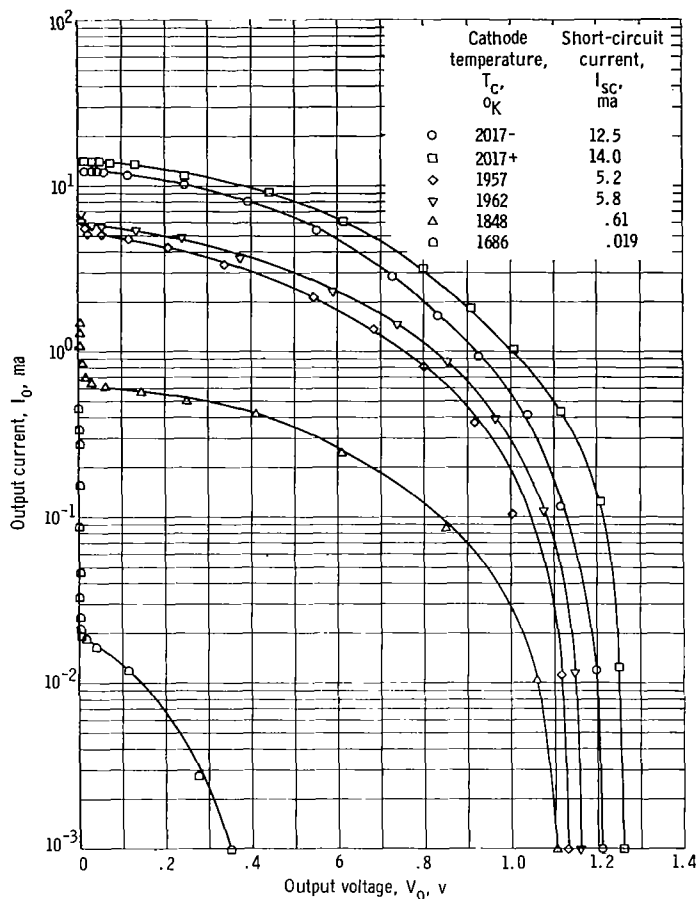
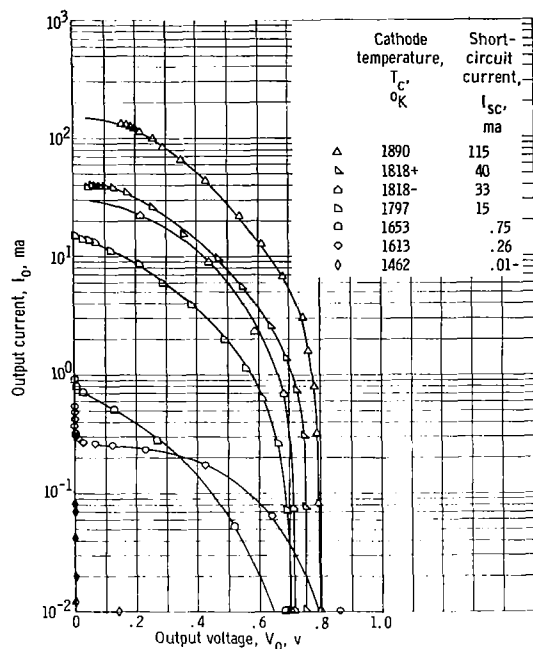


Figure 14. - Temperature variation of work function for tungsten cathode.



(a) Vacuum (air pressure, 1×10^{-4} to 3×10^{-4} torr).
Figure 15. - Thermionic output current characteristics.



(b) Cesium vapor (pressure, 5×10^{-4} torr).
Figure 15. - Concluded. Thermionic output current characteristics.

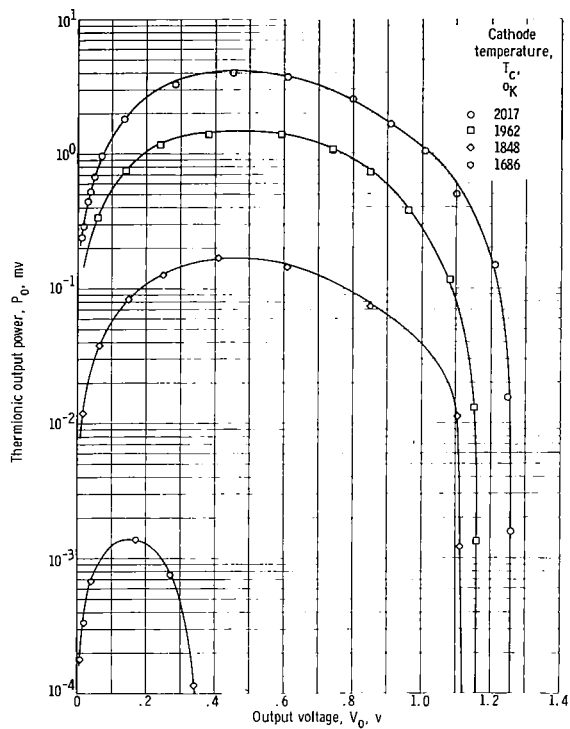
Output current I_o is plotted against V_o for a vacuum and a cesium vapor atmosphere in figure 15, while output power P_o is plotted against V_o in figure 16. Variation of open-circuit voltage V_{oc} with T_c under vacuum conditions is shown in figure 17(a) and with a cesium vapor pressure of 5×10^{-4} torr in figure 17(b).

Short-circuit current densities with a vacuum and cesium vapor were determined for comparison with the saturated emission characteristics of the tungsten cathode. Figure 18 is a plot of saturation and short-circuit current densities J_s and J_{sc} , respectively, against T .

DISCUSSION OF RESULTS

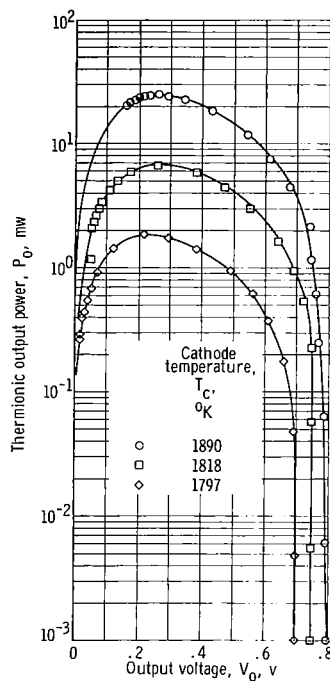
Thermal Characteristics

Effect of temperature gradients. - Because of axial temperature gradients along the electrodes, areas calculated from the physical dimensions of the electrodes could not be used in association with T_a and T_c , the maximum



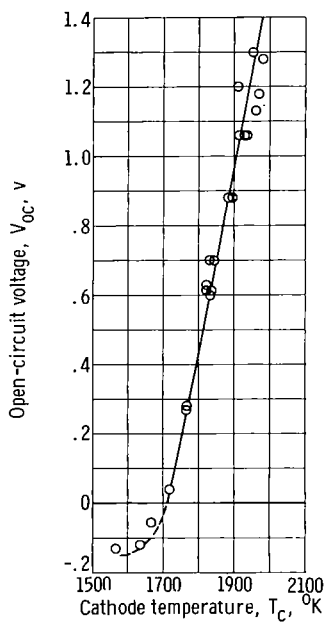
(a) Vacuum (air pressure, 10^{-4} torr).

Figure 16. - Thermionic output power characteristics.



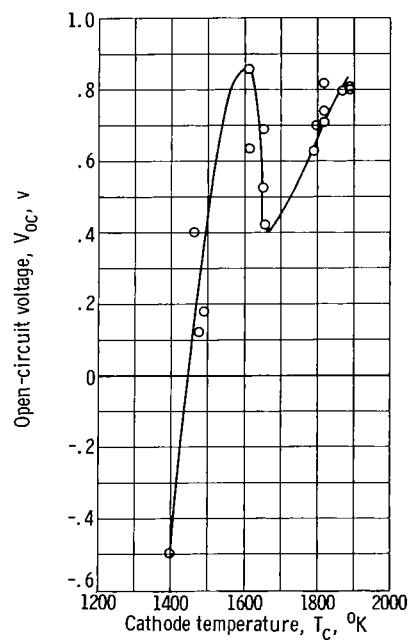
(b) Cesium vapor (pressure, 5×10^{-4} torr).

Figure 16. - Concluded. Thermionic output power characteristics.



(a) Vacuum (air pressure, 10^{-4} torr).

Figure 17. - Open-circuit voltage.



(b) Cesium vapor (pressure, 5×10^{-4} torr).

Figure 17. - Concluded. Open-circuit voltage.

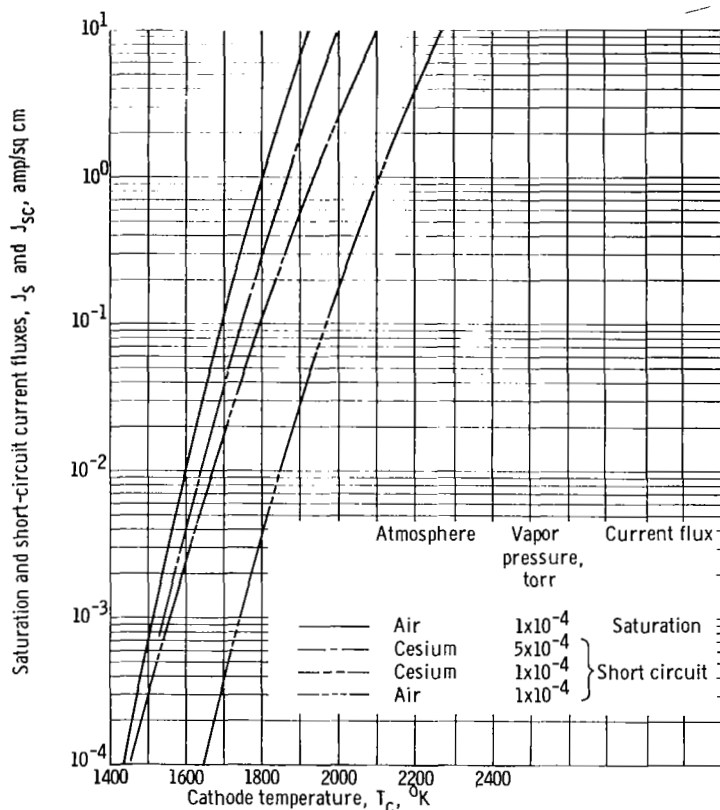


Figure 18. - Comparison of saturation and short-circuit current densities.

trode midpoint T_m . Twelve segments were used to make the summation in equation (5), and the fluxes $D(T)$ were taken from references 16 and 17.

It should be noted that equation (5) yields a fictitious area that may be used with the midpoint temperature T_m to obtain the same total heat or electron flux as that which was actually measured.

Although equation (5) is valid for thermal emission and electron emission for saturated conditions, it does not account for the fact that the distribution of electron velocities in the interelectrode space does not correspond to the maximum temperature of the electrode but rather to some lower temperature. This deviation could have a small effect on the thermionic results obtained.

The effective areas are designated by primed symbols so that A'_c , A'_a , A'_{aw} , and A'_{ce} represent, respectively, the effective areas of the cathode (thermal emission), anode (thermal emission), anode outer surface (thermal emission), and cathode (electron emission). These areas are tabulated in table II.

Temperature ratios. - As shown in figure 8, the temperature ratios T_a/T_c and T_c/T_h varied only slightly from a mean value of approximately 0.83 for

temperatures of the anode and cathode, respectively.

Adjusted or effective values for these areas were determined from the electrode temperature profiles for a series of T_c and T_a by the following method. The length of the emitting area was divided into n equal segments, and the average temperature T_i of the i^{th} segment was estimated by using the temperature profiles such as figure 9. The effective area could then be determined from the expression

effective area =

$$\left(\text{measured area} \right) \left[\frac{1}{n} \sum_{i=1}^n \frac{D(T_i)}{D(T_m)} \right] \quad (5)$$

where $D(T)$ is the heat (or electron) emission flux for the electrode at the temperature of the i^{th} segment T_i or the maximum temperature at the elec-

TABLE II. - EFFECT OF ELECTRODE TEMPERATURE
GRADIENTS ON EMITTING AREAS

Nominal area, sq cm (a)		Effective emitting area, sq cm (b)					
			Cathode temperature, T_c , °K				
			1200	1400	1600	1800	2000
A_a	87.2	$A_a^†$	86	86	85	84	81
A_{aw}	93.5	$A_{aw}^†$	92	92	91	90	87
A_c	73.7	$A_c^†$	72	71	70	68	65
A_c	73.7	$A_{ce}^†$	57	56	55	55	54
A_c	73.7	$^c A_{ce}^†$	55	52	51	50	49

^aBased on physical dimensions of electrodes.

^bCalculated by means of eq. (5).

^cWith heat shields removed from each end of diode (presented for comparison only).

T_c ranging from 1200° to 2000° K. The near constancy of these temperature ratios can be explained in terms of the thermal properties of the emitter and the following heat-transfer relations.

The heat radiated from the cathode to the anode Q_{ca} is given by

$$Q_{ca} = \sigma \mathcal{F}_e A_c^† (T_c^4 - T_a^4) \quad (6)$$

where σ is the Stefan-Boltzmann constant, and the configuration factor for radiant heat transfer between concentric cylinders \mathcal{F}_e is given by

$$\mathcal{F}_e = \left[\frac{1}{\epsilon_c} + \frac{A_c^†}{A_a^†} \left(\frac{1}{\epsilon_a} - 1 \right) \right]^{-1} \quad (7)$$

The heat radiated from the cathode to the anode can also be written as

$$Q_{ca} = Q_{aw} + Q_{al} \quad (8)$$

where Q_{al} is dependent on the geometry of the support structure and must be determined from temperature measurements along the anode leads and supports while Q_{aw} is given by

$$Q_{aw} = \sigma \epsilon_{aw} A_{aw}^* T_a^4 \quad (9)$$

(See ref. 18 for eqs. (6), (7), and (9).)

Letting $R = T_c/T_a$ and combining equations (6), (8), and (9) result in the expression

$$R = \left[\frac{\frac{\mathcal{F}_e}{\epsilon_{aw}} \frac{A_c^*}{A_{aw}^*} \left(1 - \frac{Q_{al}}{Q_{ca}} \right)}{1 + \frac{\mathcal{F}_e}{\epsilon_{aw}} \frac{A_c^*}{A_{aw}^*} \left(1 - \frac{Q_{al}}{Q_{ca}} \right)} \right]^{1/4} \quad (10)$$

This equation demonstrates the near constancy of R with respect to T_c because it is the fourth root of a quantity involving the factors A_c^*/A_{aw}^* , $\mathcal{F}_e/\epsilon_{aw}$, and $1 - (Q_{al}/Q_{ca})$, which are all of order unity and only slightly temperature dependent at high temperatures. In fact, a 100-percent variation in the quantity $\frac{\mathcal{F}_e}{\epsilon_{aw}} \frac{A_c^*}{A_{aw}^*} \left(1 - \frac{Q_{al}}{Q_{ca}} \right)$ produces only a 5-percent variation in R .

Thermal emissivities. - A variation of 50 percent in emissivity and, hence, in total radiation intensity or heat flux is possible with variations in the physical state of the emitting surface (ref. 19). This suggests that ϵ_{aw} and \mathcal{F}_e , a function of ϵ_c and ϵ_a , should be determined experimentally for the exact materials under anticipated conditions if any reasonably accurate estimate of the heat transferred is desired.

This conclusion has been borne out in this investigation. Table III lists the values of \mathcal{F}_e and ϵ_{aw} determined from equations (6) and (9), respectively, and also the values of these quantities based on published data (refs. 16 and 17). Note that the disagreement in most instances exceeded even the 50-percent figure mentioned previously. This is true even if the 10-percent error associated with the calorimetry is considered (see appendix C).

TABLE III. - THERMAL FLUXES AND EMISSIVITIES

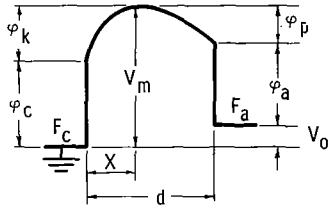
Cathode temperature, T_c , °K	Anode temperature, T_a , °K	Anode emissivity, ϵ_{aw}		Configuration factor, \mathcal{F}_e	
		Measured (a)	Published (b)	Measured (a)	Published (b)
1400	1190	0.18	0.12	0.58	0.065
1700	1430	.30	.18	.44	.11
2000	1620	.39	.21	.41	.14

^a Determined by means of eqs. (6) and (9).

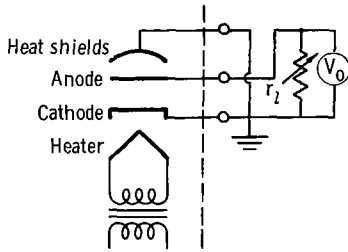
^b Taken or calculated from values published in refs. 16 and 17.

Thermionic Characteristics

Mathematical model. - The electron potential diagram and the circuit diagram for the diode are shown in figures 19(a) and (b), respectively (ref. 4). The cathode and anode work functions are φ_c and φ_a , respectively. The maximum value of the electron space charge potential between cathode and anode is represented by V_m . The distance of the potential maximum from the cathode surface is X , and d is the radial distance from cathode to anode. The cathode and anode Fermi levels are F_c and F_a , respectively. In the diode circuit diagram (fig. 19(b)), the output voltage and load resistance are represented by V_o and r_l , respectively.



(a) Potential diagram for thermionic diode.



(b) Circuit diagram for thermionic diode.

Figure 19. - Potential and circuit diagrams for thermionic diode.

Saturated emission current density $J_s(\varphi, T)$ is given by the Richardson-Dushman thermionic equation

$$J_s(\varphi, T) = A T^2 \exp\left(-\frac{e\varphi}{kT}\right) \quad (11)$$

where φ is electrode work function and T is temperature. The saturated emission current densities for the cathode and anode are $J_s(\varphi_c, T_c)$ and $J_s(\varphi_a, T_a)$, respectively.

For vacuum and low-pressure cesium conditions, the current density from the cathode to the anode is

$$J_{c-a} = J_s(\varphi_c, T_c) \exp\left(-\frac{e\varphi_k}{kT_c}\right) \quad (12)$$

where

$$\varphi_k = V_m - \varphi_c \quad (13)$$

and the current from the anode to the cathode (back-emission) is

$$J_{a-c} = J_s(\varphi_a, T_a) \exp\left(-\frac{e\varphi_p}{kT_a}\right) \quad (14)$$

where

$$\varphi_p = V_m - V_o - \varphi_a \quad (15)$$

The output current density is

$$J_o = J_{c-a} - J_{a-c} \quad (16)$$

Cathode emission properties. - The work function and the electron emission constant may be obtained by means of a Richardson-Dushman plot of $\ln(J_s/T^2)$ against $1/T$. The linearity of the Richardson-Dushman plot is usually taken as indicating that the work function φ is constant with respect to temperature. Since equation (11) may be rewritten as

$$\ln\left(\frac{J_s}{T^2}\right) = -\frac{e\phi}{k} \frac{1}{T} + \ln \mathcal{A} \quad (17)$$

the Richardson-Dushman slope may be interpreted as $-e\phi/k$ and the Richardson-Dushman intercept as $\ln \mathcal{A}$, from which the work function ϕ and the emission constant \mathcal{A} can be obtained.

The value of \mathcal{A} as measured by the Richardson-Dushman plot of figure 13 is 10^4 amperes per square centimeter per $^\circ K^2$ if it be assumed that ϕ_c is a constant with respect to T_c . But this assumption is unnecessary even though the Richardson-Dushman plot obtained was found to be linear. If ϕ were linearly dependent upon temperature, that is, if

$$\phi = \phi_0 + \gamma T \quad (18)$$

where ϕ_0 and γ are constants, then equation (17) would become

$$\ln\left(\frac{J_s}{T^2}\right) = -\frac{e\phi_0}{k} \frac{1}{T} + \ln \mathcal{A} - \frac{e\gamma}{k} \quad (19)$$

and a linear Richardson-Dushman plot with a slope equal to $-e\phi_0/k$ and an intercept equal to $\ln \mathcal{A} - (e\gamma/k)$ would result.

From an assumed theoretical value of 120.4 amperes per square centimeter per $^\circ K^2$ for \mathcal{A} and the measured value of the intercept, the proportionality constant γ , which gives the linear dependence of the work function on temperature, may be evaluated. The constant γ was found to be -5.1×10^{-4} volt per $^\circ K$, a value that agrees closely with those reported for tungsten in reference 20. The cathode work function based on equation (19) was 4.35 to 4.05 volts in the temperature range from 1700° to 2000° K, as opposed to the usually quoted constant value of 4.5 volts. Therefore, as shown by figure 12, the saturation current fluxes for the tungsten cathode were larger than the Jones-Langmuir values for tungsten (refs. 21 and 22).

The use of 120.4 amperes per square centimeter per $^\circ K^2$ for \mathcal{A} has a sound theoretical basis. The value 120.4 is obtained only in special cases, however, by the usual method of interpreting the Richardson-Dushman intercept as $\ln \mathcal{A}$ instead of $\ln \mathcal{A} - (e\gamma/k)$ (see ref. 23). A detailed discussion of factors influencing work function and emission constant is given in reference 24.

Short-circuit currents. - Figure 15 shows an interesting feature of the diode output characteristics: a sharp increase in I_o at values of V_o near zero volt. The increase occurred for V_o between 0 and 0.04 volt and corresponded to values of load resistant r_l below 5 ohms. As T_c was increased from 1500° to 1800° K, r_l had to be decreased from about 5 to 1 ohm to initiate the sharp increase. For T_c near 2000° K, the increase was not evident, probably because r_l 's lower than 1 ohm were not used. This sharp increase in I_o always occurred after a threshold potential of less than 0.04 volt had been reached. Factors which may have been involved in producing this anomalous effect were not investigated in this experiment.

Short-circuit current densities J_{sc} plotted in figure 18 were based on the output characteristics shown in figure 15 through the equation

$$J_{sc} = \frac{I_{sc}}{A_{ce}^{\dagger}} \quad (20)$$

The short-circuit current I_{sc} was determined from the output curves in figure 15 by extrapolating to zero voltage and disregarding the curves where the sharp increase in output current occurred.

Space-charge cancellation, or the reduction of V_m by means of cesium vapor, is evident in figure 18, in which the J_{sc} curves approach the J_s curve for the cathode with increases in cesium vapor pressure.

Open-circuit voltages. - Under vacuum conditions, the variation of the open-circuit voltage V_{oc} with T_c (fig. 17(a)) appeared to be linear except for the region in which the polarity changed from negative to positive. It should be noted that under open-circuit conditions the anode was floating and thus served as a potential probe. For negative values of V_{oc} , which occurred below 1700° K, the curve deviated from linearity and tended to level off at about 0.15 volt.

Open-circuit characteristics can be analyzed by using equation (16) in the following manner. With an open circuit $J_{c-a} = J_{a-c}$; therefore, equating the logarithms of equations (12) and (14) yields

$$(1 - R)V_m - V_o = \frac{-2RkT_c}{e} \ln\left(\frac{1}{R}\right) \quad (21)$$

where $V_m = \phi_k + \phi_c$. Letting V_{oc} represent V_o at open circuit yields

$$V_{oc} = (1 - R)V_m + \frac{2RkT_c}{e} \ln\left(\frac{1}{R}\right) \quad (22)$$

Since $V_m \geq \phi_c$ (where $\phi_c \geq \phi_a$ is assumed),

$$V_{oc} \geq (1 - R)\phi_c + \frac{2RkT_c}{e} \ln\left(\frac{1}{R}\right) \quad (23)$$

The right side of equation (23) should then provide a positive lower bound for V_{oc} .

For $T_c = 2000^\circ$ K, $R = 0.83$, $\phi_c = 4.05$ volts, and equation (23) gives $V_{oc} \geq 0.74$ volt. The observed value of V_{oc} under these conditions was 1.45 volts (fig. 17(a)), which agrees with the inequality in equation (23). For $T_c = 1700^\circ$ K, however, zero voltage was actually observed for V_{oc} whereas equation (23) requires that $V_{oc} \geq 0.73$ volt. Furthermore, equation (23) requires that V_{oc} always be positive, which is in disagreement with

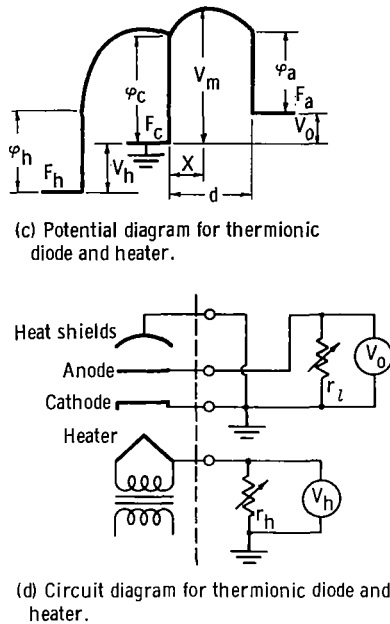


Figure 19. - Concluded. Potential and circuit diagrams for thermionic diode.

the polarity change observed.

It seems reasonable to believe that the model leading to equations (12), (14), and (16) does not incorporate the factors needed to explain the effects observed under open-circuit and short-circuit conditions.

The inflection in the open-circuit voltage curve shown in figure 17(b) is the same as that observed in other investigations under similar conditions for diodes operated with low-pressure cesium vapor (ref. 10).

Effect of heater potential. - Because electrons emitted from the heater could have contributed to the interelectrode space charge, the influence of the heater potential bias on converter operation was investigated. Figure 19(c) shows the electron potential diagram for the diode with the heater potential included. The voltage from heater to ground V_h was measured by means of an electrometer. Heater potential bias was set by a variable heater to ground resistor r_h shown in the circuit diagram in figure 19(d).

During normal output operations the heater floated with respect to ground. In figure 20(a) a plot of the heater floating potential V_h against cathode temperature T_c with r_h approximately infinity is shown. The variation of V_h against T_c with r_h set at 1.2 ohms is shown in figure 20(b). In this case the heater and cathode formed a diode system that carried about 2 amperes

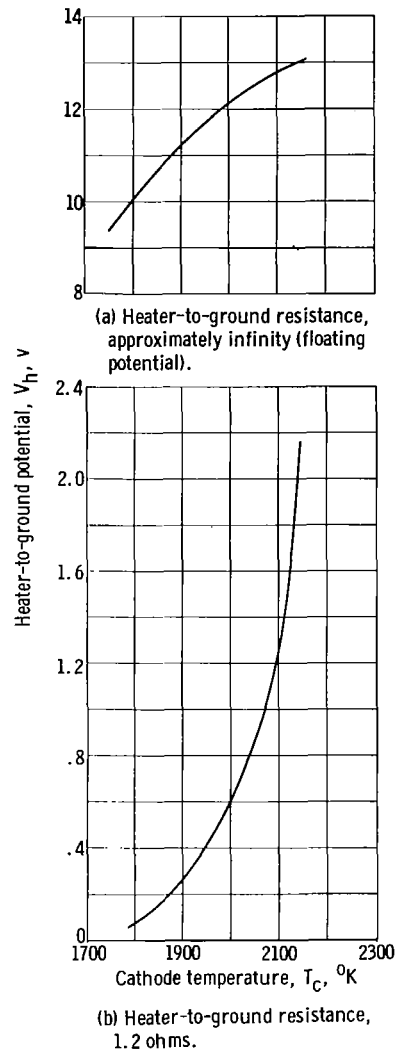


Figure 20. - Heater potential.

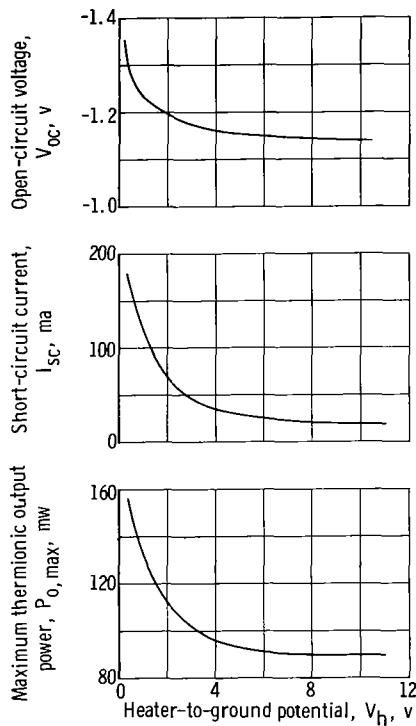


Figure 21. - Effect of heater potential on open-circuit voltage, short-circuit current, and maximum power output. Cathode temperature, 2125°K .

at T_c equal to 2150°K .

Lowering the heater-to-ground resistance r_h effected substantial increases in V_{oc} , I_{sc} , and P_o , shown

in figure 21. Dropping V_h from its floating value of 13 volts to 0.2 volt caused a twofold increase in maximum output power $P_{o,max}$. It was also observed that varying the diode output current I_o between the cathode and the anode by changing r_l had no discernible effect on the heater potential. Thus, it was seen that, although V_h did have a marked effect on the converter output in the diode design studied, it was itself unaffected by variations in output current and voltage.

Effects of metallic vapor deposition. - After long-term operations of the diode for 20 to 80 hours at cathode temperatures of 1700° to 2000°K , an appreciable amount of electrode materials was found to have deposited on cooler components. This metallic vapor deposition was serious enough to alter the work function of the anode and to change the electrical properties of ceramic insulators.

A layer of tungsten estimated to be several atoms thick had deposited on

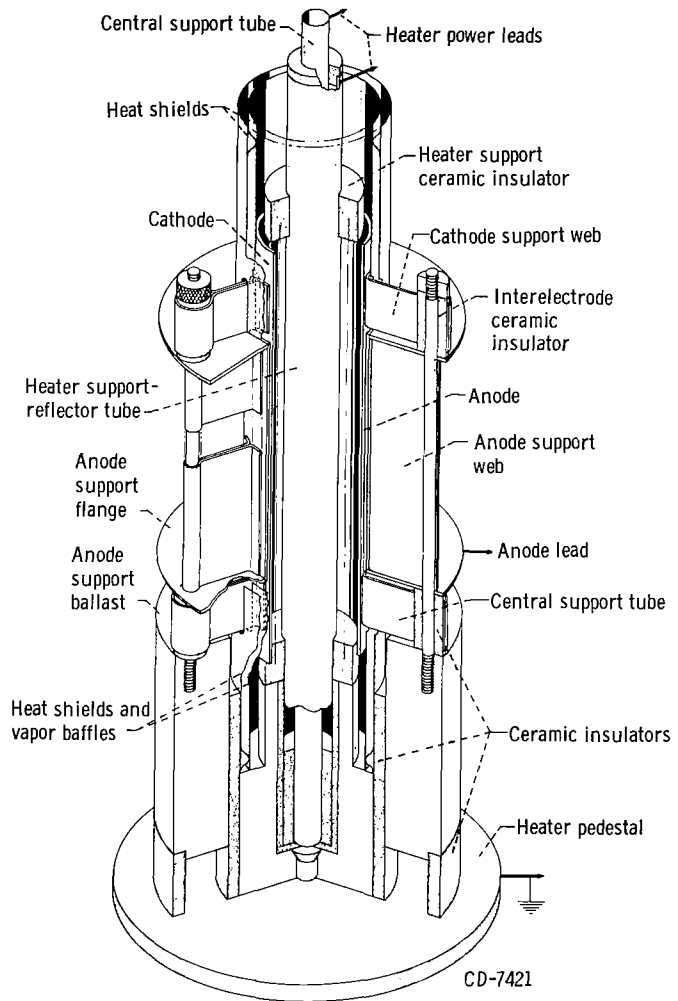


Figure 22. - Converter model B.

the anode collecting surface after a 20-hour period with T_c equal to 2000° K. As the deposition progressed, the work function of the tantalum anode changed until it became nearly the same as that of the tungsten cathode.

Metallic vapor deposition on ceramic parts such as interelectrode insulators was found to have serious consequences especially in the earlier version of the diode designated as model B (fig. 22). In model B interelectrode insulators consisting of alumina cylinders positioned and supported the electrodes. To avoid vapor contamination, these insulators were located outside the hot zone and were protected by heat shields, which also served as optical vapor baffles. In spite of these precautions the insulators degenerated rapidly, and the interelectrode resistance dropped from a value exceeding 5 megohms to 1000 ohms after operation for about 20 hours with the cathode at 2000° K. Although this interelectrode resistive leakage did not change the diode characteristics, it did affect the applied voltage characteristics I_p against V_p . Consequently, it was necessary to revise the converter design to the one shown in figure 4, in which the ceramic interelectrode insulators were even farther from the hot zone.

Because of its importance in long-term diode operations, the nature of the vapor deposition on ceramic parts in model B was closely examined. Figure 23

shows photographs of the heater and interelectrode alumina insulators used in model B before and after contamination. Spectroscopic and X-ray diffraction analyses indicated moderate to trace amounts of copper, iron, tungsten, and tantalum against the alumina background. Spectroscopic analysis of the material used in the fabrication of the tungsten cathode showed the presence of copper in trace amounts and iron in amounts between 50 and 100 parts per million. Thus, the more volatile impurities in the tungsten may have been prominent in producing the depositions.

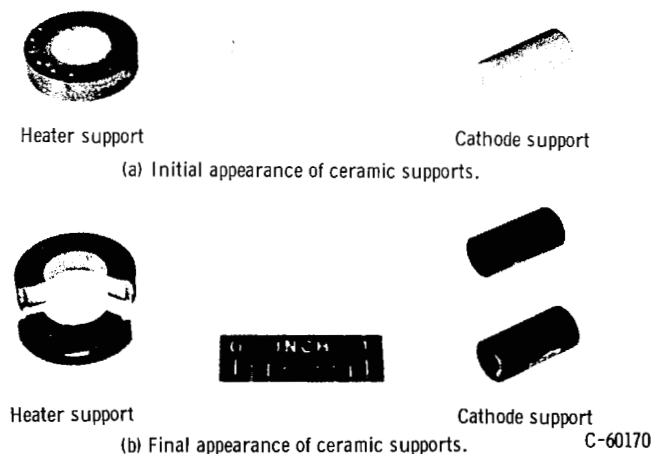


Figure 23. - Vapor deposition of metallic film on ceramic interelectrode insulators in converter model B.

The dependence of the interelectrode leak resistance for model B upon duration of operation in the cathode temperature range 1800° to 2000° K over a 20-hour period was determined and found to be approximately

$$\lambda = 10^5 \exp(-0.08 t) \quad (24)$$

If equation (24) holds for longer periods, after 200 hours the leak resistance λ would be of the order of 10^{-2} ohm, and converter output characteristics would certainly be adversely affected.

Designs that have been proposed for nuclear-powered thermionic conversion systems require a closely packed arrangement of insulators and electrodes to reduce void space (refs. 3 and 25). In such systems metallic vapor deposition, which can seriously hamper power output, may not be as easily circumvented as in the present case, in which the interelectrode insulators were placed far from the hot zone.

SUMMARY OF RESULTS

An experimental thermionic diode converter was described. The device was designed for an investigation of problems associated with heating and instrumenting a large-scale converter and for a determination of certain thermal and thermionic characteristics. Among the thermal characteristics determined were electrode temperature ratios, temperature gradients, heat-flow distribution, and heat-emission properties. Thermionic characteristics that were determined included vacuum and low-pressure cesium vapor outputs, electron-emission properties, effects of heater potential, and effects of metallic vapor deposition on electrical insulators. The following results were obtained:

1. With the anode being cooled exclusively by means of radiant heat transfer to a 100° F heat sink, the anode-to-cathode temperature ratio remained nearly constant at 0.83 for cathode temperatures ranging from 1200° to 2000° K.

2. Thermal emissivities determined for the electrode materials by means of heat-flow measurements disagreed with published values by more than 50 percent.

3. Effective electrode emitting areas associated with thermal and thermionic emission were reduced by as much as 30 percent over actual physical emitting areas for cathode temperatures in the range 1200° to 2000° K because of temperature gradients along the electrodes.

4. Vapor deposition of the cathode and heater materials on the anode effected a change in the anode work function. Metallic vapor deposition also changed the electrical insulating properties of ceramic insulators and caused interelectrode resistance to drop by several orders of magnitude in a 20-hour period.

5. The vacuum work function of the tungsten cathode varied from 4.35 to 4.05 volts as the cathode temperature varied from 1700° to 2000° K as opposed to the usually accepted constant value of 4.5 volts for tungsten.

Lewis Research Center

National Aeronautics and Space Administration
Cleveland, Ohio, September 5, 1963

APPENDIX A

SYMBOLS

A_a	measured nominal inner area of anode, sq cm
A_a^t	inner effective thermal emission area of anode, sq cm
A_{aw}	measured outer area of anode, sq cm
A_{aw}^t	outer effective thermal emission area of anode, sq cm
A_c	measured area of cathode, sq cm
A_c^t	effective thermal emission area of cathode, sq cm
A_{ce}^t	effective thermionic emission area of cathode, sq cm
A	Richardson-Dushman emission constant, 120.4 amp/(sq cm)(°K) ²
C	transmission constant, eq. (D1)
c	specific heat, Btu/(lb)(°F)
$D(T)$	thermal or thermionic emission flux at temperature T_i , w/sq cm or amp/sq cm
d	radial spacing between cathode and anode, mm
e	electronic charge, 1.60×10^{-19} coulomb
F_a	anode Fermi level
F_c	cathode Fermi level
F_h	heater Fermi level
\mathcal{F}_e	configuration factor, eq. (10)
G	flow rate, gal/min
I_o	output (or net) current, ma
I_p	plate current under applied voltage, ma
I_s	saturation current under applied voltage, ma
I_{sc}	short-circuit current, ma
i	i^{th} statistical segment, eq. (5)

J_{a-c}	current flux from anode to cathode, amp/sq cm
J_{c-a}	current flux from cathode to anode, amp/sq cm
J_O	output (or net) current flux, amp/sq cm
J_S	saturation current flux, amp/sq cm
J_{sc}	short-circuit current flux, amp/sq cm
k	Boltzmann constant, 1.3805×10^{-23} j/°K
l	leak resistance between cathode and anode, ohms
n	number of statistical segments, eq. (5)
P_e	thermal energy carried away from cathode by electrons (includes thermionic power output P_O), kw
P_h	heater input power, kw
P_l	power lost in heater leads, kw
P_O	thermionic output power, mw
p_1	silicone fluid pressure at pump outlet, lb/sq in.
p_2	silicone fluid pressure at upstream flowmeter, lb/sq in.
p_3	silicone fluid pressure at downstream flowmeter, lb/sq in.
Q_{al}	heat conducted in anode leads, kw
Q_{aw}	heat radiated anode to enclosure wall, kw
Q_{ca}	heat radiated from cathode to anode, kw
Q_{cl}	heat conducted in cathode leads, kw
Q_{cw}	heat radiated from cathode to enclosure wall, kw
Q_{hl}	heat conducted in heater leads, kw
Q_l	heat conducted in leads, eq. (3), kw
Q_m	heat absorbed by heat-exchange manifold, eqs. (4) and (C1), kw
Q_{ra}	heat radiated axially to enclosure wall, kw
R	ratio of anode to cathode temperature, T_a/T_c

r_h resistance from heater to grounds, ohms
 r_l load resistance, ohms
 T temperature, $^{\circ}\text{K}$
 T_a anode midpoint or maximum temperature, $^{\circ}\text{K}$
 T_c cathode midpoint or maximum temperature, $^{\circ}\text{K}$
 T_e silicone fluid manifold entrance temperature, $^{\circ}\text{F}$
 \bar{T}_f mean temperature of silicone fluid in manifold, $^{\circ}\text{F}$
 ΔT_f silicone fluid temperature difference across manifold, $T_o - T_e$, $^{\circ}\text{F}$
 T_{fm} silicone fluid temperature at flowmeter, $^{\circ}\text{F}$
 T_h heater temperature, $^{\circ}\text{K}$
 T_i temperature of i^{th} statistical segment, eq. (5), $^{\circ}\text{K}$
 T_m midpoint or maximum temperature of electrode (equal to T_a or T_c),
eq. (5), $^{\circ}\text{K}$
 T_o silicone fluid manifold outlet temperature, $^{\circ}\text{F}$
 T_{ob} observed absolute temperature, $^{\circ}\text{K}$
 t time, hr
 V_h potential from heater to ground, v
 V_m electron potential maximum, $\phi_c + \phi_k$, v
 V_o output voltage, v
 V_{oc} open-circuit voltage, v
 V_p applied (or plate) voltage, v
 w specific gravity
 X distance from cathode to potential maximum, V_m , mm
 α constant, eq. (4)
 β constant, eq. (4)
 γ work-function temperature constant, eq. (18), $\text{v}/^{\circ}\text{K}$

ϵ_a	total thermal emissivity of anode collecting surface
ϵ_{aw}	total thermal emissivity of anode outer surface
ϵ_c	total thermal emissivity of cathode emitting surface
θ	true absolute temperature, $^{\circ}\text{K}$
σ	Stefan-Boltzmann constant, $5.67 \times 10^{-12} \text{ w}/(\text{sq cm})(^{\circ}\text{K}^4)$
ϕ	work function, v
ϕ_a	anode work function, v
ϕ_c	cathode work function, v
ϕ_h	heater work function, v
ϕ_k	difference between V_m and ϕ_c , eq. (13), v
ϕ_o	Richardson-Dushman work function, eq. (18), v
ϕ_p	difference between V_m and $\phi_a + V_o$, eq. (15), v

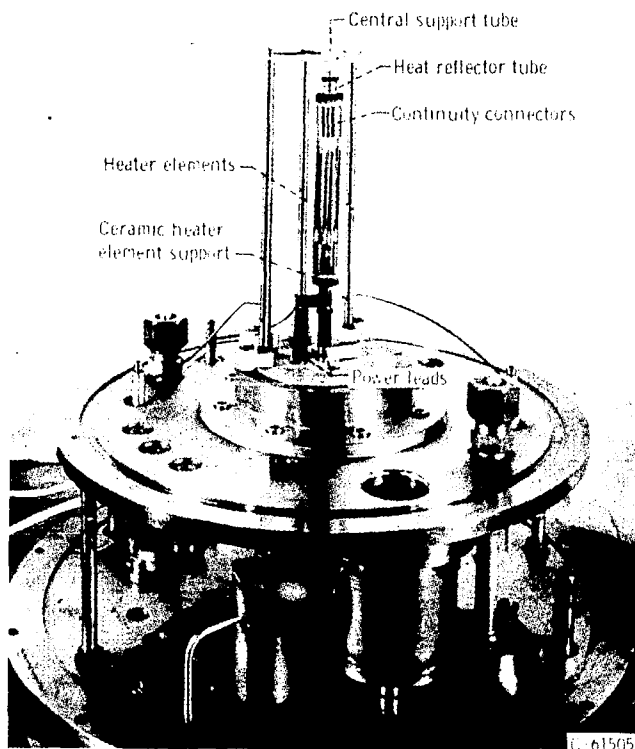
APPENDIX B

CATHODE HEATER

General Description

A refractory-metal radiative heater was designed to heat the cathode. The heater was contained within the cathode cylinder and had a maximum operating

temperature of over 2500° K. The heat generation capacity was in excess of 4 kilowatts. The impedance of the heater was relatively high, and 4 kilowatts could be generated with a current of less than 60 amperes. The mode of construction was such that the ceramic supports and insulators were located entirely outside the high-temperature zone with only refractory-metal components located within. Heater elements were shaped tantalum strips fastened together with tantalum connectors. The elements were arranged to cancel magnetic flux by means of opposite currents in adjacent elements.



(a) Cathode heater installed on base plate.

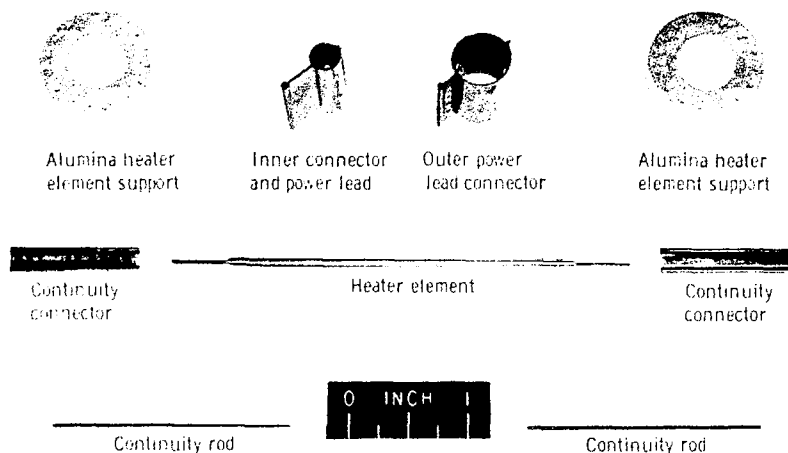
Figure 24. - Heater, components, and characteristics.

A drawing of the heater appears in figure 5, and a photograph showing the heater installed on the vacuum base plate appears in figure 24(a). Various heater components are displayed in figure 24(b). The following dimensions characterized the heater:

Overall height (including heater element supports), cm	15.2
Overall diameter, cm	2.54
Mean diameter of high-temperature zone, cm	2.10
Length of high-temperature zone, cm	10
Nominal heat-radiating area, sq cm	60
Mean radial distance to cathode, mm	3.4
Electrical resistance at room temperature, ohms	0.5 to 1.0

Construction Details

All the metallic portions were tantalum, while the insulator supports consisted of magnesium silicate and alumina.



C-65372

(b) Tantalum and alumina heater components.

Figure 24. - Continued. Heater, components, and characteristics.

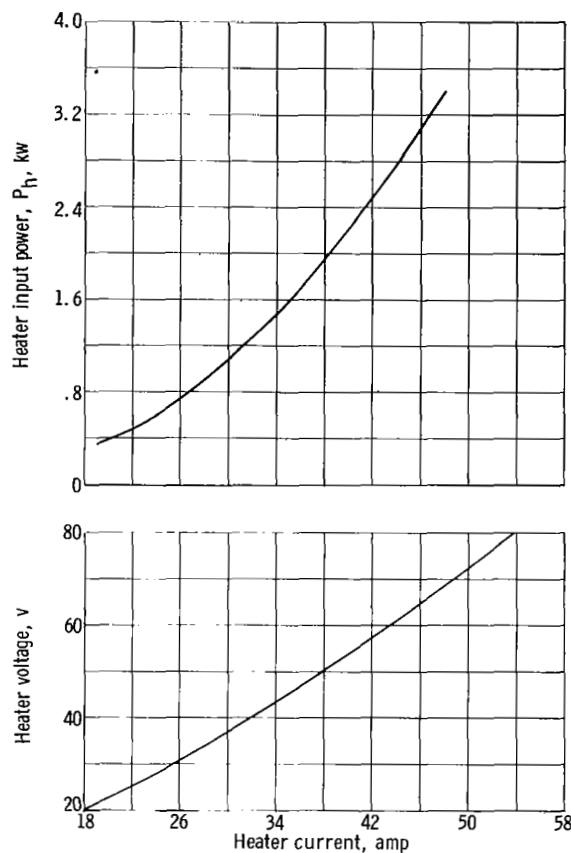
The heater elements were formed from 16 tantalum strips 4 inches long, 3/16 inch wide, and 10 mils thick, which were bent about their major center-lines to a dihedral angle of 60° (fig. 24(b)). At each end a 1/2-inch section was formed to receive a 40-mil-diameter tantalum continuity rod. Continuity connectors formed from 10-mil tantalum sheet were used to join the elements by engagement with the continuity rods. Sixteen heater elements were thus connected to form a cylindrical configuration as shown in figure 5.

Spacing, support, and insulation were provided by ceramic parts, the most important of which were the two heater element supports shown in figure 24(b). The element supports, which were annular in shape, had a 1/2-inch inside diameter, a 1-inch outside diameter, and a 1/2-inch height. Each had a set of 16 holes for receiving the extreme ends of the continuity rods, and the holes were equally spaced on a 7/8-inch-diameter circle.

Two 10-mil wall coaxial tantalum tubes composed the underlying support structure and also served as electrical leads. The inner or central support tube, which was 1/4 inch in diameter and 10 inches in length, ran through the center of the heater assembly and was joined to one of the elements by the inner power lead connector as shown in figure 5. The second tube or heat reflector, which was 1/2 inch in diameter and 8 inches in length, was coaxial with and insulated from the central support tube. The heat reflector was joined to a second heater element by means of the outer power lead connector. Inner and outer power lead connectors are illustrated in figure 24(b).

Operating Characteristics

The heater was powered by 60-cycle alternating current drawn from a 20-kilovolt-ampere transformer. The heater output was quite stable, and only minor voltage adjustments were required to maintain the power level over 8- to



(c) Heater characteristics.

Figure 24. - Concluded. Heater, components, and characteristics.

10-hour periods.

Figure 24(c) shows typical heater characteristics in terms of heater power input P_h , heater voltage, and heater current. The relation between P_h and heater temperature T_h is plotted in figure 7.

Measurements of the slope of the heater voltage against current plot at various points were used to gage the variation of heater resistance with temperature. This was compared with the thermal variation of the resistivity of tantalum, and the close correspondence between the two was taken to indicate that contact resistance among the numerous heater components was negligible.

Cancellation of Magnetic Flux

To determine the effectiveness of the flux-cancelling geometry, a full-size mockup of the heater was constructed. A gauss meter was used to map the resultant field density adjacent to the mock heater elements. With the gauss-meter probe at a radial distance of 3 millimeters from the lateral surface of the mock heater, directly opposite an element and oriented

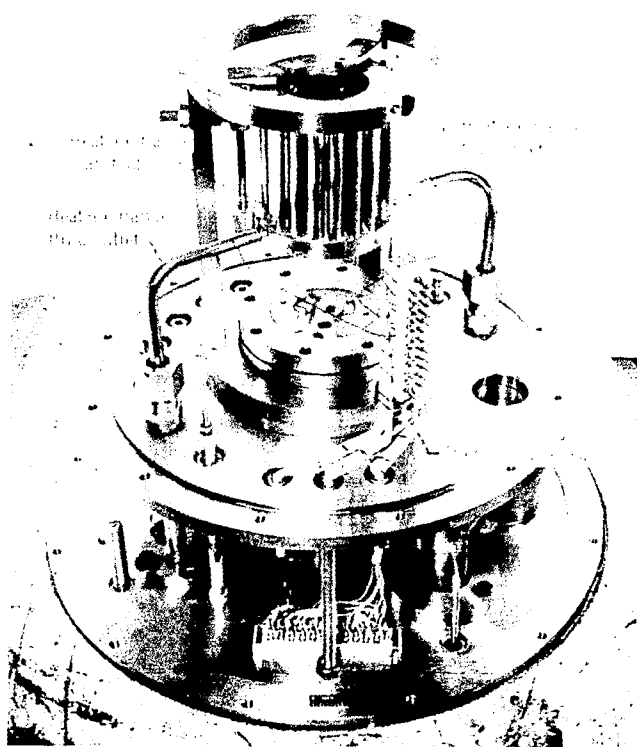
to intercept maximum flux, the density registered was 2 gauss at 50 amperes. (Note that this was the field density in the interelectrode space between the cathode and anode for the diode.) The reference flux density for 50 amperes adjacent to a long straight wire was 17 gauss for an equivalent probe orientation.

APPENDIX C

HEAT-EXCHANGE SYSTEM

System and Components

The main components of the heat-exchange system were the heat-exchange manifold, the gear pump, the turbine flowmeter, and the cooling coils. Dimethyl silicone fluid (ref. 26) was used as the heat-transfer medium because of its low vapor pressure at high temperatures. Figure 25(a) is a photograph of the heat-exchange manifold installed on the vacuum base plate. A schematic diagram of the system is shown in figure 25(b).



(a) Manifold installed on base plate.

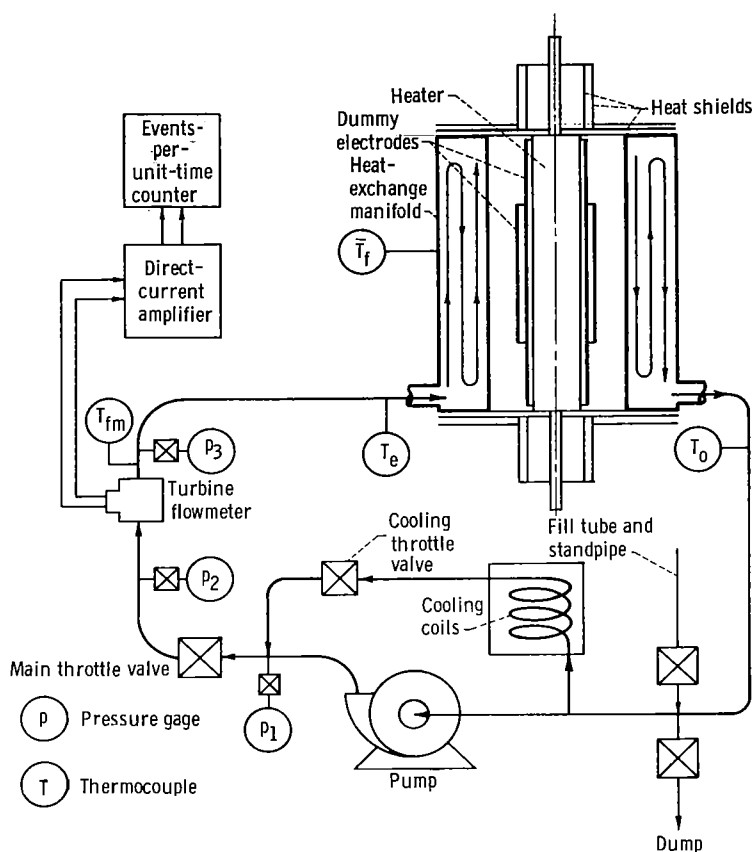
Figure 25. - Heat-exchange system.

The heat-exchange manifold consisted of a number of stainless-steel tubes arranged to form a cylinder, 6 inches high, having a 5-inch outside diameter and a 3-inch inside diameter. The tubes were connected by a manifold to provide flow as shown in figure 25(b). When used for heat-flow studies, the heat-exchange manifold was installed coaxially with the heater-electrode centerline. A turbine flowmeter was used to measure flow rates. The flowmeter output voltage pulsations were fed through an amplifier and counted on an events-per-unit-time indicator. The fluid was circulated by means of a gear pump rated at 18 gallons per minute and 1.5 horsepower. A water-cooled bypass coil was provided for temperature regulation.

Flow Measurement

The calibration of the flowmeter consisted of determining its calibration factor in cycles per gallon, as a function of its output pulsation in cycles per

second, for a range of fluid viscosities between 10 and 40 centistokes. This procedure was followed because it was necessary to operate the flowmeter at 25 to 50 percent of rated capacity in a region in which the calibration factor was highly dependent on viscosity. It was undesirable to operate above 50 percent of capacity because the higher operating pressures involved would have taxed the system unnecessarily.



(b) Schematic diagram of system.

Figure 25. - Concluded. Heat-exchange system.

temperatures at various points (fig. 25(b)), the thermocouple wells were provided to ensure accurate gaging of fluid temperatures. The measurements made were fluid temperature at the manifold inlet, fluid temperature at the manifold outlet, and average fluid temperature in the manifold. At least two thermocouples were used at each location to check temperatures. The average fluid temperature in the manifold was used to determine the specific weight and heat of the fluid for use in equation (C1). This temperature was checked by comparison with $1/2(T_0 + T_e)$.

The error involved in the measurement of Q_m was found to be 10 percent by direct calibration. This value agreed closely with the estimated error that was determined by using assumed errors for the various factors involved in equation (C1).

Parametric plots of cycles per gallon against cycles per second were made for a series of values of viscosity ranging from 10 to 40 centistokes. The calibration factor cycles per gallon was determined by interpolation of the curves of cycles per gallon against cycles per second. The appropriate viscosity was taken from a plot of viscosity against temperature by means of temperatures provided by a thermocouple just downstream of the flowmeter (T_{fm} in fig. 25(b)).

Calorimetry

The heat absorbed by the heat-exchange fluid Q_m was determined by

$$Q_m = 5.272 \times 10^{-2} \text{ wcG } \Delta T_f \quad (C1)$$

Iron-constantan thermocouples measured system tem-

APPENDIX D

TEMPERATURE DETERMINATION

Optical Pyrometer Measurements

The primary means for determining electrode temperature was a monochromatic micro-optical pyrometer with an operating wavelength of 0.665 micron. Three measurements were made in gaging electrode temperatures:

(1) A series of 1/64- by 3/64-inch-deep hohlraums (blind holes) were provided on the cathode and the anode (fig. 1). The brightness temperatures of these hohlraums were corrected for window absorption and recorded directly with the assumption of an emissivity factor of unity.

(2) The brightness temperatures of points between and adjacent to the hohlraums were measured, corrected for window absorption, and converted to "true" temperatures by using the brightness temperatures as guides in estimating appropriate spectral emissivity factors.

(3) Check measurements were made by using tungsten-rhenium thermocouples in cavities and on the walls adjacent to the hohlraums. These measurements served as further guides in estimating appropriate spectral emissivity factors.

To convert the surface brightness temperatures to true temperatures for tungsten electrodes, a conversion curve based on data published in reference 16 was plotted. For tantalum electrodes the conversion curve was based on data compiled in references 19 and 27. Window corrections were computed from

$$\frac{1}{\theta} - \frac{1}{T_{ob}} = \frac{\log C}{9588} \quad (D1)$$

where θ is the true absolute temperature, T_{ob} is the observed absolute temperature, and C is the transmission constant of the glass. The transmission constant of the glass used in these experiments was determined to be about 0.9 by direct calibration.

Thermocouple Measurement

A means of checking optically determined temperatures was provided by the use of rhenium-tungsten thermocouples. A small cavity was provided on the electrode surface near the hohlraum for the thermocouple junction such that the junction was about one-half contained. The junction was held in place solely by spring loading. A second rhenium-tungsten thermocouple adjacent to the first was merely held against the electrode surface to provide a check. Measurements were also made with the thermocouples interchanged as a further check. The temperature values were based on Lachman and McGurty's calibrations for the tungsten-rhenium system (ref. 28).

Accuracy and Reliability

Typical results for the three methods are presented in figure 26, in which corrected values are plotted against heater current. These measurements were made at the center hohlraum of the cathode.

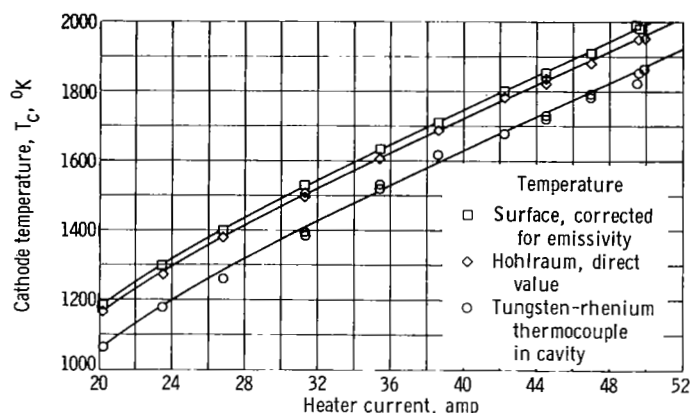


Figure 26. - Comparison of temperature measuring techniques.

The two sets of optically determined values agreed within 1.6 and 1.5 percent at 1200° and 2000° K, respectively. The maximum error of the optical pyrometer was estimated to be less than 0.5 percent in this range, and, therefore, the discrepancies may be attributed in part to errors associated with the values used for emissivity and window corrections. These errors appear to have been systematic, but nevertheless, the results of the two measurements were in good agreement. It is noteworthy that the difference between the hohlraum and surface temperature curves in figure 26 does not diverge at the

higher temperatures in spite of the somewhat shallow hohlraums. The 3-to-1 depth-to-diameter ratio of hohlraums did not appear to affect the accuracy of the temperature measurements significantly. Both the hohlraum and emissivity-corrected surface temperatures were so close that either could be taken for the true value without seriously affecting calculations dependent on them.

The discrepancy between the optical and thermocouple measurements ranged from 8 to 5 percent over the interval 1200° to 2000° K, and the thermocouple measurements were consistently lower by about 100° K. This discrepancy was probably due to errors caused by radiation and conduction heat losses from the thermocouple junction.

Heater Temperatures

The determination of the heater temperatures (i.e., heater element temperatures) proved to be somewhat difficult. An optical pyrometer was used to gage the temperatures, but, because hohlraum cavities could not be provided in the thin heater elements, the temperature measurements depended on assumed emissivity factors.

By observing the heater parallel to its axis (through the top view port, fig. 6(b)), certain portions of the heater elements could be seen edgewise. Inasmuch as the surfaces of the elements had a matte finish, the temperatures were judged to be accurate to within 20° K. If the temperature profile for the heater was similar to that observed for the cathode, the measured end tempera-

ture was probably within 50° to 100° K of the temperature at the midpoint of the heater elements. The heater temperature measurement was further corroborated by comparing measured and published (refs. 17 and 19) heat fluxes for tantalum at various heater temperatures determined by the optical method.

REFERENCES

1. Slone, Henry O., and Lieblein, Seymour: Electric Power Generation Systems for Use in Space. *Advances in Aero. Sci.*, vol. 4, Th. Von Kármán, et al., eds., Pergamon Press, 1961, pp. 1131-1152.
2. Evvard, J. C.: Electric Space Propulsion. *Electrical Eng.*, vol. 79, no. 7 July 1960, pp. 555-562.
3. Bernatowicz, Daniel T.: A Parametric Study of the Thermionic Diode System for Large Nuclear-Electric Powerplants in Space Vehicles. NASA TN D-1110, 1962.
4. Nottingham, W. B.: Thermionic Diode as a Heat-to-Electrical-Power Transducer. *Jour. Appl. Phys.*, vol. 30, no. 3, Mar. 1959, pp. 413-417.
5. Lewis, H. W., and Reitz, J. R.: Thermoelectric Properties of the Plasma Diode. *Jour. Appl. Phys.*, vol. 30, no. 9, Sept. 1959, pp. 1439-1445.
6. Wilson, Volney, C.: Conversion of Heat to Electricity by Thermionic Emission. *Jour. Appl. Phys.*, vol. 30, no. 4, Apr. 1959, pp. 475-481.
7. Houston, J. M.: Theoretical Efficiency of the Thermionic Energy Converter. *Jour. Appl. Phys.*, vol. 30, no. 4, Apr. 1959, pp. 481-487.
8. Hatsopoulos, G. N., and Kaye, J.: Analysis and Experimental Results of a Diode Configuration of a Novel Thermoelectron Engine. *Proc. IRE*, vol. 46, no. 9, Sept. 1958, pp. 1574-1579.
9. Grover, G. M., Roehling, D. J., Salmi, E. W., and Pidd, R. W.: Properties of Thermoelectric Cells. *Jour. Appl. Phys.*, vol. 29, no. 11, Nov. 1958, pp. 1611-1612.
10. Pidd, R. W., et al.: Characteristics of a Plasma Thermocouple. *Direct Conversion of Heat to Electricity*, J. Kaye and J. A. Welsh, Eds., John Wiley & Sons, Inc., 1960, pp. 10-1 - 10-12.
11. Steele, Howard: Energy Converters Using Low-Pressure Cesium. *Direct Conversion of Heat to Electricity*, J. Kaye and J. A. Welsh, eds., John Wiley & Sons, Inc., 1960, pp. 11-1 - 11-9.
12. Ranken, W. A., Grover, G. M., and Salmi, E. W.: Experimental Investigation of the Cesium Plasma Cell. *Jour. Appl. Phys.*, vol. 31, no. 12, Dec. 1960, pp. 2140-2153.
13. Auer, Peter L.: Potential Distributions in a Low-Pressure Thermionic Converter. *Jour. Appl. Phys.*, vol. 31, no. 12, Dec. 1960, pp. 2096-2103.
14. Pidd, R. W., et al.: Research on Cesium-Vapor Cells Employing Carbide Cathodes. Rep. GA-1973, Summary Rep. May 1, 1960 - Jan. 31, 1961, General Atomic, Feb. 7, 1961.

15. Ingold, J. H., and Tonks, Lewi: Plasma as a Thermocouple Leg. Rep. R6OAPF9 (GEAP-3484), General Electric Co., Dec. 31, 1960.
16. Smithells, Colin James: Tungsten, Its Metallurgy, Properties, and Applications. Chem. Pub. Co., Inc., 1953.
17. Ogden, H. R.: Physical and Mechanical Properties of Tantalum. DMIC Memo. 32, Defense Metals Info. Center, Aug. 28, 1959.
18. Jakob, Max: Heat Transfer. Vol. II. John Wiley & Sons, Inc., 1957.
19. Schmidt, F. F.: Tantalum and Tantalum Alloys. DMIC Rep. 133, Battelle Memorial Inst., July 25, 1960.
20. Hutson, Andrew R.: Velocity Analysis of Thermionic Emission from Single-Crystal Tungsten. Phys. Rev., vol. 98, no. 4, May 1955, pp. 889-901.
21. Barth, V. D.: Physical and Mechanical Properties of Tungsten. DMIC Rep. 127, Defense Metals Info. Center, Mar. 15, 1960.
22. Jones, H. A., and Langmuir, I.: The Characteristics of Tungsten Filaments as Functions of Temperature. Gen. Electric Rev., vol. 30, no. 6, June 1927, pp. 310-319.
23. Shelton, Haywood: Thermionic Emission from a Planar Tantalum Crystal. Phys. Rev., vol. 107, no. 6, Sept. 1957, pp. 1553-1558.
24. Herring, Conyers, and Nichols, M. H.: Thermionic Emission. Rev. Modern Phys., vol. 21, no. 2, Apr. 1949, pp. 185-270.
25. Harvey, R. J.: Summary Report of Thermionic Isotopic Power System. Martin Co., MND-P 2399, Nuclear Div., 1960.
26. Anon.: Silicones - Product Data. Silicone Fluids, SF-96 ser., rev. B, General Electric Co.
27. Smithells, Colin J.: Metals Reference Book. Vol. II. Butterworths Sci. Pub., 1955.
28. Lachman, J. C., and McGurty, J. A.: Refractory Metal Thermocouples. Paper 59-HT-21, ASME, 1959.